

Dynamics of the perfect storms: La Niña and Australia's extreme rainfall and floods of 1974 and 2011

Jennifer Whelan¹  · Jorgen S. Frederiksen¹

Received: 5 October 2015 / Accepted: 8 August 2016 / Published online: 27 October 2016
© Springer-Verlag Berlin Heidelberg 2016

Abstract An ensemble of general circulation model simulations and dynamical mode analyses of important weather systems contributing to Australia's severe rainfall and flooding events, in January 1974 and January 2011, are described. Dispersion relation techniques have also been used to extract the leading weather systems in observations and general circulation model (GCM) simulations, including Kelvin waves and intraseasonal oscillations. We find that the severe rainfall and flooding events over northern Australia in January 1974 and January 2011 coincided with significant intraseasonal oscillation and Kelvin wave activity that constructively interfered on the critical days of very high rainfall. The CSIRO Mk3L spectral GCM has been used to simulate both events. Particular simulations from 1870 to 2011, forced by observed SSTs and increasing CO₂, agree well with observations in both the timing and patterns of these disturbances. The growth and structures of the leading dynamical normal modes have also been determined within a two-level primitive equation instability model. Our results show explosively growing intraseasonal oscillations and atmospheric Kelvin waves convectively coupled in the Australian monsoonal region. Monsoon disturbances, associated blocking over the Tasman Sea, and tropical–extratropical interactions also significantly contributed to the heavy rainfall. Model simulations and analyses of the dynamical modes are consistent with the synoptic situation seen in observational data for both severe precipitation events, and provide a more complete description of the reasons for the extreme impact of both events.

Keywords La Niña · Extreme events · Flooding · Simulations · Kelvin waves · Intraseasonal oscillations

1 Introduction

Australia's highly variable climate is uniquely vulnerable to the El Niño Southern Oscillation (ENSO) (e.g., Philander 1990; McBride and Nicholls 1983; Nicholls et al. 1997; Wang and Hendon 2007). While North America experiences drier conditions during La Niña periods, Australia may be suffering widespread flooding; likewise, strong El Niños bring widespread drought to Australia while North America may be drenched. Understanding ENSO and the nature of these extreme events over Australia is especially critical in the cases of severe droughts or flooding that devastate lives, homes, and industry, as it is a fundamental step in the pursuit of accurate predictions of future ENSO impacts and Australia's future climate and climate extremes.

In this paper, we examine changes in the basic climate state over Australia during the two severe rainfall and flooding periods of January 1974 and January 2011. According to the Australian Bureau of Meteorology website,¹ the years 1973–1976 and 2010–2012 are considered the two most severe La Niña periods in terms of precipitation and flooding in Australia since 1900. The largest floods occurred during January 1974 and late December 2010 through January 2011, in both cases flooding the Queensland, including Brisbane, and New South Wales coastal areas, and in the latter case causing floods inland and south down to Victoria. ENSO metrics such as the Southern

✉ Jennifer Whelan
Jennifer.Whelan@csiro.au

¹ CSIRO Oceans and Atmosphere, 107-121 Station Street, Apsendale, VIC 3195, Australia

¹ <http://www.bom.gov.au/climate/enso>.

Oscillation Index (SOI—the difference in sea level pressure between Darwin and Tahiti) indicate the severity of ENSO conditions with extreme SOIs of 27 and 28 preceding the 1974 and 2011 floods. However, metrics do not necessarily indicate the extent of impact (Wang and Hendon 2007); nor do they offer an understanding of the dynamical conditions causing the widespread impact seen in both events.

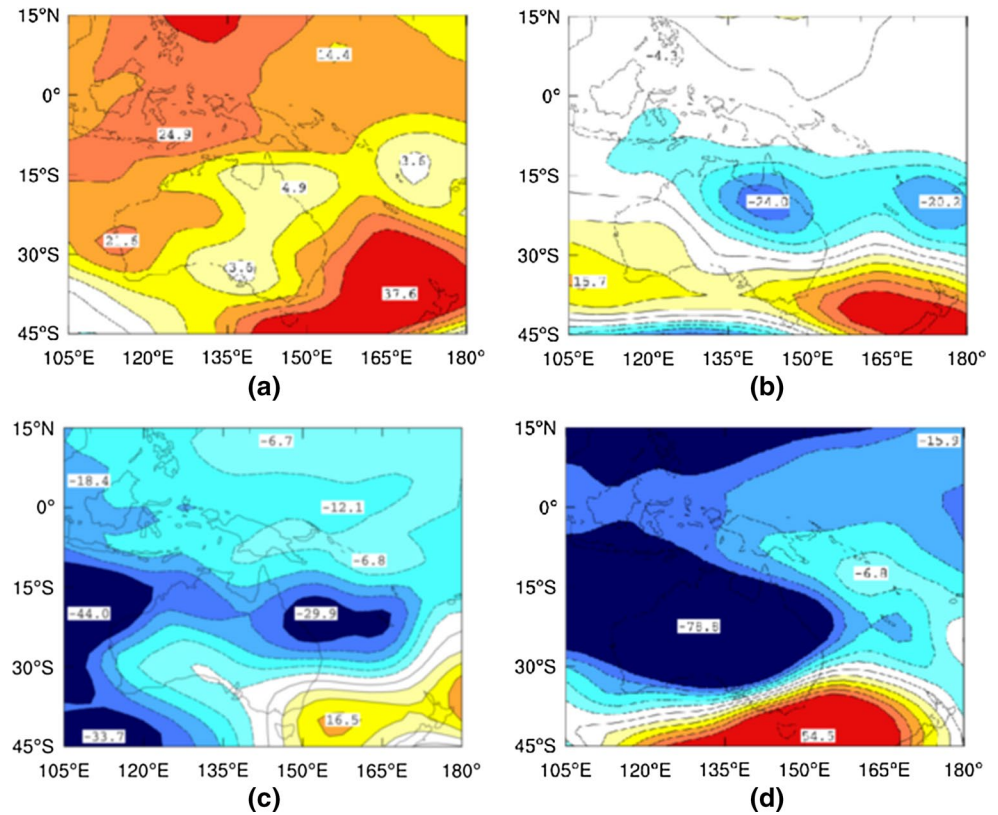
There has been extensive research on ENSO going back decades, but less work has been done on the causes of circulation features associated with La Niña phases in the southern hemisphere (SH) or Australia specifically. Karoly (1989) described general SH circulation features during El Niño conditions. Others have looked at the relationship between ENSO and the Southern Annular Mode (SAM) and Antarctic sea ice extent in the SH (e.g., L'Heureux and Thompson 2006; Pezza et al. 2008). Most of the wide range of research looking at the Madden Julian Oscillation (MJO; Madden and Julian 1971) and ENSO focuses on the MJO contribution to El Niño conditions (Hendon et al. 2007; Moon et al. 2011), although Wheeler et al. (2009) showed that the MJO was a main driver of rainfall in northern Australia and could also influence rain in the extratropics over the austral summer. The tropical–extratropical interactions of the MJO have been well documented, as reviewed for example by Frederiksen and Lin (2013). A recent study by Moteki (2016) documents the interaction of the MJO with extratropical cyclone activity in the southern hemisphere. The Indian Ocean Dipole (IOD) is also known to have a distinct relationship with Australian rainfall (Nicholls 1989; Ashok et al. 2003; Meyers et al. 2007). Risbey et al. (2009) considered ENSO, IOD, MJO, SAM and blocking as drivers of Australian rainfall, all having seasonal and geographically-varying influences. Brown et al. (2009) showed that precipitation impacts of El Niño phases were modulated by the number and behaviour of cutoff low pressure systems over Australia. The type of El Niño (or La Niña) also affects the extent of the negative (positive) precipitation anomaly (Wang and Hendon 2007; Taschetto and England 2009; Cai and Cowan 2009).

In recent years there have also been important insights into aspects of the 2010–2012 La Niña. Cai and van Rensch (2012) show that January 2011 severe rainfall marked a transition to the negative phase of the Pacific Decadal Oscillation, which typically brings with it a higher level of rainfall. The contributing role of local sea surface temperature (SST) anomalies and circulation to the severe precipitation in northeast Australia during 2010–2011 was studied by Evans and Boyer-Souchet (2012), Ummenhofer et al. (2015) and Whelan and Frederiksen (2015). Lewis and Karoly (2015) established robust relationships for a substantial La Niña influence on Australian rainfall during 2010–2012.

Frederiksen and Frederiksen (2005, 2007) have previously elucidated the role of weather systems in climate regime change and shown that changes in the growth and structures of storms explain the significant rainfall reduction in southwest Western Australia since the mid-1970s. Frederiksen and Frederiksen (2011) also determined that the causes of the southern Australian Millennium Drought of 1997–2006 (extending to 2009), associated with some medium to strong El Niño events, were due to changes in weather systems. In this paper, we present a first systematic comparison of commonalities between the compound severe rainfall and extreme flooding events of 1974 and 2011. In particular, we compare observed anomalous SSTs, atmospheric circulation, rainfall and OLR over the summer seasons, growth and changes in the Madden-Julian Oscillation, the role of tropical–extratropical interactions, and the roles of interacting Kelvin waves and MJO disturbances in observations and simulations with the CSIRO model of the two events. These complementary avenues of analysis offer a more complete explanation and case studies of the reasons behind the extensive impacts of the severe precipitation events associated with two of the most extreme flooding events in Australia's recent history.

The plan of this paper is as follows. Section 2 summarises the synoptic conditions over Australia typical of the different phases of ENSO, and details the January 1974 and January 2011 rainfall events and floods. Section 3 describes the data sets used in analysis of rainfall, OLR and weather systems and circulation. The data analysis methods of extracting the important atmospheric waves and oscillations contributing to the severe rainfall and flooding events are summarised in Sect. 4. The focus is on determining the periods and wave number ranges of Kelvin waves and the MJO and establishing their roles in the severe rainfall events during January 1974 and January 2011. In Sect. 5, the simulations of the January 2011 and 1974 high rainfall events with the CSIRO Mk3L global climate model forced by observed SSTs are described. A standard or baseline simulation (STD-FORCED) is described as well as methods for generating members of an ensemble (FORCED) of simulations. Comparisons are made between the observations and simulations. The methods of determining the dynamical modes based on a primitive equation instability model are summarized in Sect. 6; leading dynamical modes associated with the La Niña of 1974 are described in Sect. 6.1 and corresponding disturbances for the 2011 La Niña are presented in Sect. 6.2. The relationships between the dynamical modes such as Kelvin waves and intraseasonal oscillations obtained from a primitive equation instability model, and those obtained from wavenumber-frequency filtering of OLR anomalies in Sect. 4, are described. Our conclusions are presented in Sect. 7.

Fig. 1 Geopotential height anomalies (m) at 700 hPa highlight the circulation differences between El Niño and La Niña periods over Australia and show the severity of the January 1974 and 2011 conditions. **a** El Niño January 1998, **b** moderate La Niñas (composite of Jan 2008 and 2009), **c** January 2011 La Niña and **d** January 1974 La Niña. Contour interval: 5 hPa



2 Synoptic description of La Niña extreme precipitation events

There are considerable changes in the near equatorial circulation during the ENSO cycle. In neutral and El Niño conditions, there is higher pressure and geopotential height over the Indian Ocean, Australia and the western Pacific than in La Niña years (Fig. 1). Typically, a high can be seen in the geopotential height at 700 hPa over the Indian Ocean that extends east over western and central Australia, driving winds in an anticyclonic pattern from the Indian Ocean eastward across the south Australian coast, curving around northward to create an easterly flow across the northern half of Australia. During La Niña conditions, however, this high over Australia is usually either smaller or non-existent. In 1974, there was a large low pressure system over Australia and in 2011 there were negative pressure anomalies over the Indian Ocean and Australia (Fig. 1).

2.1 January 1974

According to the Australian Bureau of Meteorology,² 1974 is the wettest year on record, with 1973 the 3rd and 1975 the 5th wettest. In particular, Australia experienced the

heaviest flooding in its recorded history during January 1974. Figure 2a shows rainfall anomalies across Australia for the month, with some areas receiving more than twice their average annual rainfall in January alone. One catchment near Brisbane received 1300 mm in 5 days. Inland areas remained submerged for months in some areas.

A westerly anomalous flow built over the Indian Ocean along the equator in October and November 1973, and extended over Indonesia in December, gaining strength. At the same time, the trade winds weakened below the equator west of 180E. By January the tropical westerly winds gained further strength and extended south, following a low-pressure ridge along the north and east coasts. These winds displaced the weak high pressure system to the south, and the mid-latitude westerlies only covered Tasmania. Winds converged off the east coast to create an area of confluence and unstable easterly winds across Australia. Both these, plus blocking highs in the Tasman Sea, served to trap the convection over Australia and prevent it moving off into the Pacific. Additional moisture was made available through the pairing of a negative IOD with anomalous high SSTs in the Indian Ocean and tropical Pacific (Figs. 2a, 3a).

2.2 January 2011

During the period 2010–2012, precipitation totals were second only to those for 1973–1976; area-averaged rainfall

² <http://www.bom.gov.au/climate/current/special-statements.shtml>.

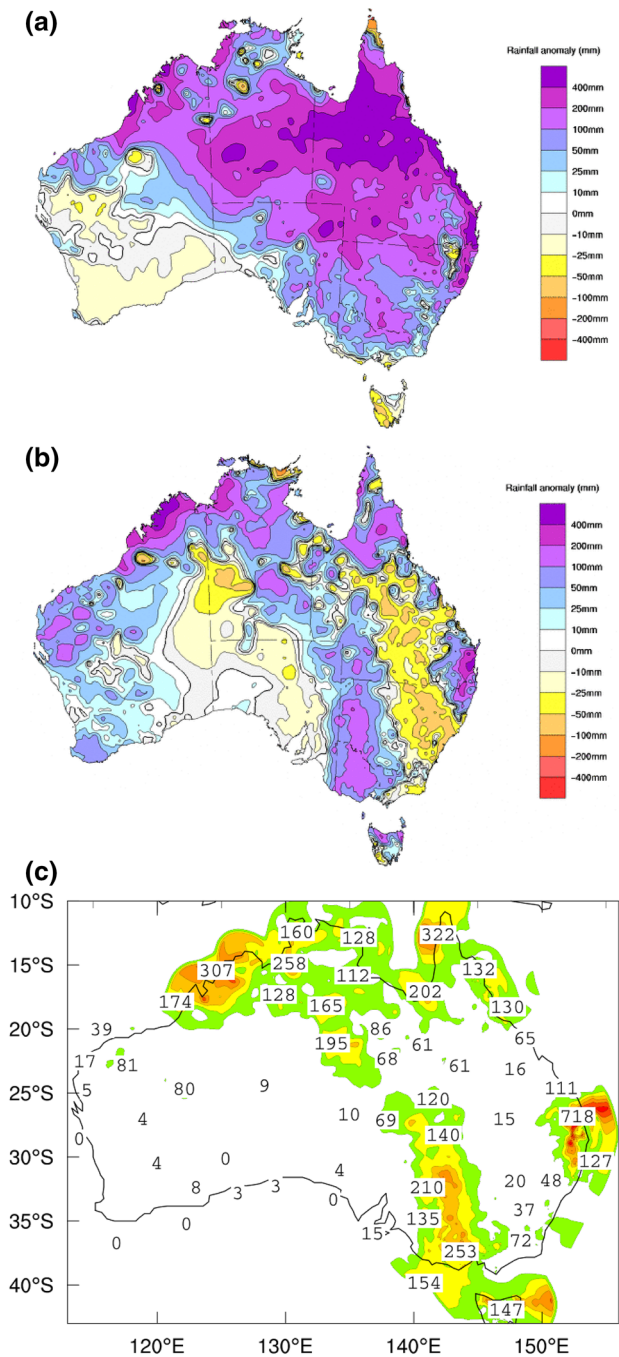


Fig. 2 Rainfall anomalies (mm) over Australia from the Australian Bureau of Meteorology¹ for **a** January 1974, **b** January 2011 and **c** AWAPS station data totals (mm) from January 9 to 14, 2011 (Jones et al. 2009). These observational data show the concentrations and extent of the anomalous precipitation. In January 2011, we focus on the mid-January severe rainfall (**c**), which makes up, to a large extent, the anomalous precipitation for the month (**a**). Contour interval in (**c**): 50 mm

totals over Australia were 1402 mm, very near the area-averaged 1407 mm total for 1973–1974. The strong La Niña of 2010–2011 receded between May and September

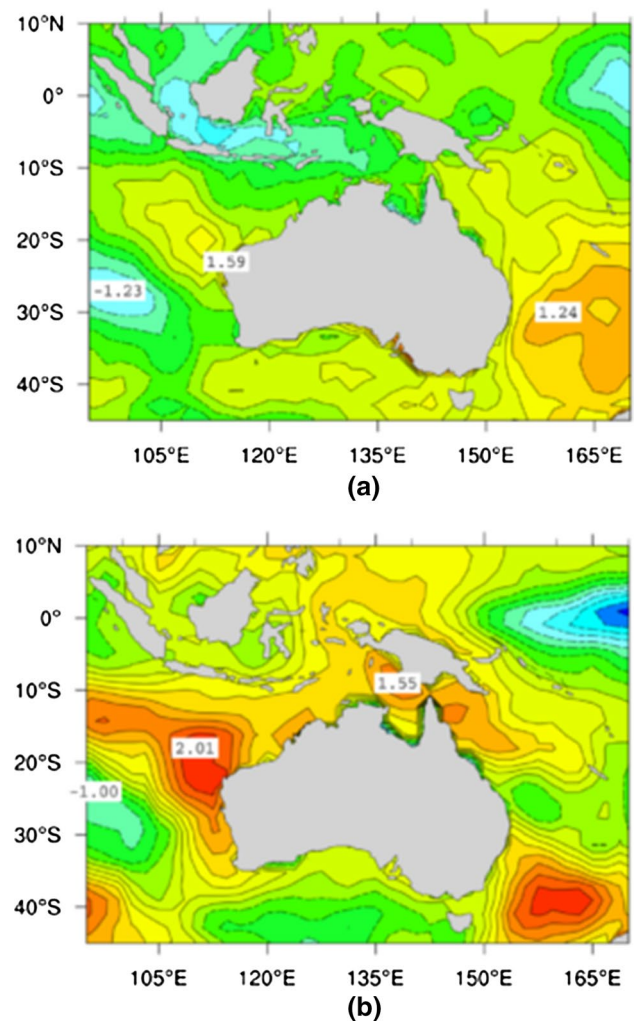


Fig. 3 SST anomalies (°C) during **a** December 1973, preceding January 1974 and **b** December 2010, preceding the January 2011 Australian floods. Contour interval: 0.25 °C

2011. However, a second La Niña subsequently developed, and by the end of 2011 rainfall was above average for over two-thirds of Australia.

The most extreme flooding occurred in late December 2010 to January 2011 (Fig. 2b). The flooding events in January had such an extreme impact due to a build-up of moisture both in the atmosphere and the soil from the earlier heavy precipitation in December 1973.

Northerly winds and easterly flow near the coasts were caused by low pressure troughs over Australia (Fig. 1c) and a chain of blocking high pressure systems in the Tasman Sea. There was a strongly negative IOD with unusually high SSTs around Australia (Fig. 3b), which contributed to increased convection. Late December saw multiple Queensland stations setting all-time daily rainfall records from cyclone Tasha coupled with moist easterly flow (Evans and Boyer-Souchet 2012). The tropical moisture

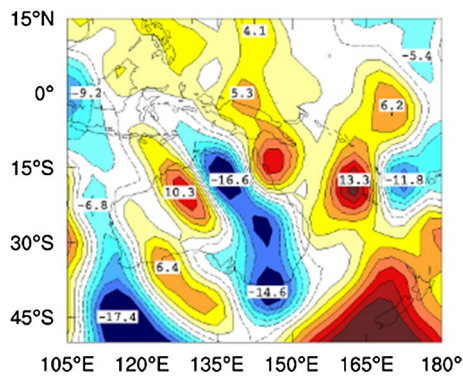


Fig. 4 The 700 hPa meridional wind on 12 January 2011, from NCEP reanalysis, highlighting the tropical–extratropical interactions. Contour intervals: 2 m/s

reached southeast Queensland and northeast New South Wales on January 10, with daily precipitation totals reaching 298 mm at one station in southern Queensland. Meanwhile, a slow-moving trough over Victoria retained the tropical moisture, resulting in record humid conditions for Melbourne. Victoria received its entire summer's average rainfall in the 6 days of January 9–14 (Fig. 2c), due to blocking high pressure systems south of Tasmania stalling the low pressure system over Victoria.

During January 2011, tropical westerly winds originating in the Indian Ocean and extending through Indonesia were drawn down from the equator into areas of lower pressure in northern and eastern Australia, due to the absence of the usually strong anticyclonic flow. They brought with them large amounts of tropical moisture. Tropical–extratropical interactions played an important role, particularly around 12 January 2011, when the southerly 700 hPa meridional wind (Fig. 4) extended from the tropics to south of Tasmania over the eastern half of Australia. The meridional wind was largely equivalent barotropic while the zonal wind in this region was westerly, including in the upper troposphere, allowing Rossby wave dispersion (Webster and Holton 1982; Frederiksen and Webster 1988). The tropical westerly winds stay around 3–4 m/s during neutral or El Niño years; in contrast, they grew to 10 m/s during January 1974 and were also anomalously strong in 2011. The tropical westerly winds differ in their paths between La Niña periods as well. In the La Niña year of 2008, the Winds were drawn out to a low over the western Pacific in 2008, while during the 1999 La Niña there was typical lower pressure over the Indian and Pacific Oceans but a strong enough high over Australia to block the subtropical westerly winds from extending over Australia.

Next we examine the role of weather systems associated with the extreme precipitation and the extreme impact of the Australian flooding during the January 1974 and 2011 La Niñas. Events of extreme impact such as major floods

can be the result of a particular variable, such as rainfall, having an extreme value. However, more frequently an extreme impact event is caused by a confluence of factors that reinforce each other even though individually they may not necessarily be extreme (Leonard et al. 2013).

3 Data

We use the Australian Water Availability Project (AWAP) 0.05 degree (5 km) interpolated daily station data (Jones et al. 2009) for determining precipitation totals over land during the extreme flooding events of January 2011 (Fig. 2c). With the grid-point analysis technique used in AWAP there is some smoothing in regions with a high density of stations, but nevertheless it is the most objective data source for extreme precipitation totals. For all other observational analyses we use the NCEP/NCAR Reanalysis I, which combines assimilated observational data from a number of different sources with numerical prediction model output to fill otherwise data-sparse regions (Kalnay et al. 1996). While reanalysis data shows smoothing and loss of the extremes of the precipitation during both 1974 and 2011, it provides global coverage of OLR and other upper level meteorological fields (Liebmann and Smith 1996). However, daily NCEP OLR is not available prior to June 1974 (therefore absent for our time of interest in January 1974). In its place we considered the 20th Century Reanalysis Version 2 (20CRV2) data set (Compo et al. 2011), which covers 1974, for examining MJO growth and propagation (Oliver and Thompson 2012).

4 Wavenumber-frequency filtering

In addition to synoptic observations, we can examine the severe flooding event of January 2011 by looking at convectively coupled equatorially-trapped waves—namely Kelvin waves—and intraseasonal oscillations such as the Madden-Julian Oscillation (MJO) (Madden and Julian 1971, 1994), both of which play critical roles in the Australasia region with effects extending poleward, through tropical–extratropical interactions, from their equatorial path. Wheeler and Kiladis (1999) describe a method of filtering selected frequencies from outgoing long wave radiation (OLR) anomaly data—OLR being a proxy for cloudiness and convection—to identify several types of equatorially trapped waves and the MJO.

Hovmöller (time-longitude) diagrams for both daily NCEP reanalysis OLR data and Mk3L simulation OLR data (covered in Sect. 5) for the period of December 2010 to February 2011, and for the Mk3L simulation OLR data from December 1973 to February 1974, are shown in

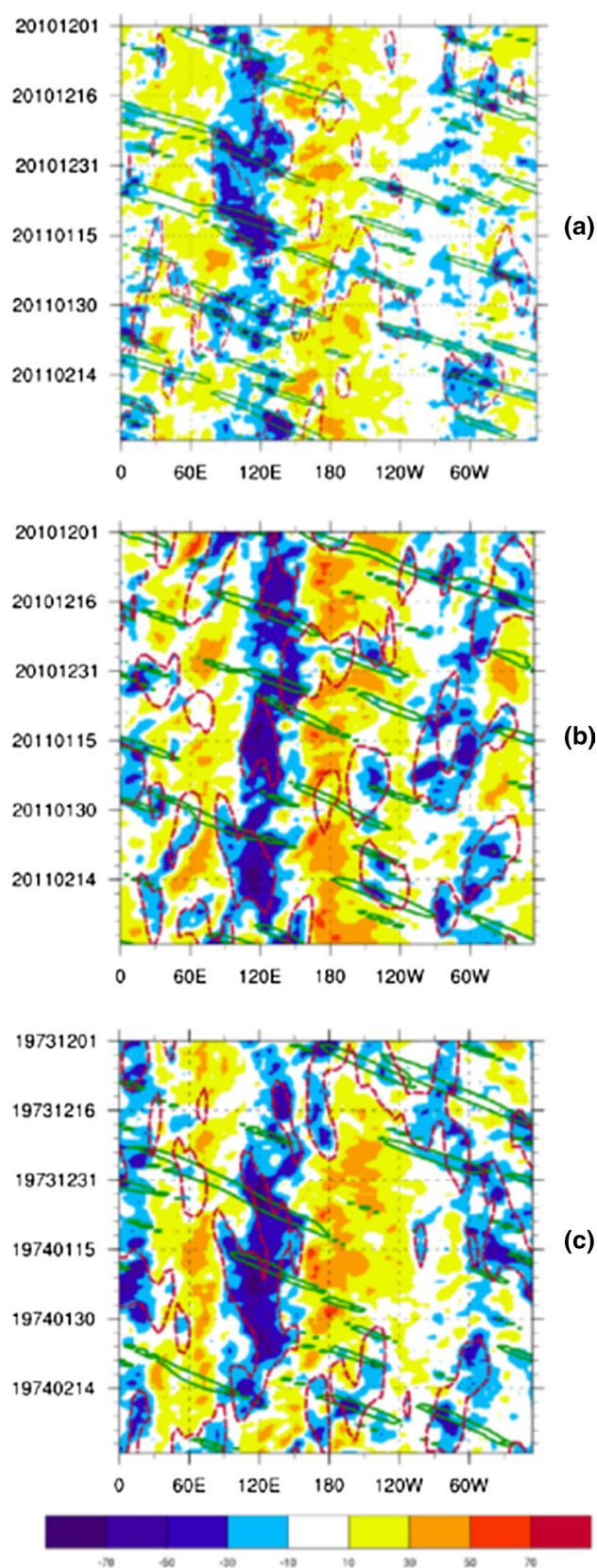
Fig. 5 Hovmoller time-longitude diagrams of OLR (Wm^{-2}) anomalies averaged over 15N to 15S covering the period **a** December 2010 to February 2011 based on NCEP data, **b** December 2010 to February 2011 from the Mk3L STD-FORCED simulation and **c** December 1973 to February 1974 from the Mk3L STD-FORCED simulation. Kelvin waves shown by *solid green contours* (contour interval 7 Wm^{-2}) and MJO in *red dashed contours* (contour interval 10 Wm^{-2}). Background is OLR anomalies, with dark colors being areas of enhanced convection. Constructive interference of the Kelvin waves and MJO can be seen in mid-January in (a) and (c), and in late January in (b)

Fig. 5. Following Wheeler and Kiladis (1999), OLR was averaged over 15N–15S, encompassing the typical areas of tropical convection and paths of the zonally propagating waves. We filtered the OLR data for both Kelvin waves (period of 2.5–20 days, zonal wavenumbers 1–14) and the MJO (period of 30–96 days, zonal wavenumbers 1–5) (from Wheeler and Kiladis (1999)). Patterns of suppressed (yellow) and enhanced (blue) convection typical of the MJO can be seen in both figures across the Indo-Pacific region. Negative OLR anomalies can be seen in the Indonesian area and north of Australia (around 120E) for the entire period. Filtered frequency bands of enhanced convection associated with the MJO are contoured in dashed red, and Kelvin waves are contoured in green. Figure 5a shows Kelvin wave peak convection coinciding with the MJO convection in the vicinity of northern Australia during early to mid-January, consistent with the extreme rainfall experienced in mid-January over Australia (Fig. 2b, c).

Tropical–extratropical interactions associated with MJO convection, reinforced by Kelvin wave convection, appear to play important roles during the peak rainfall events over northeastern and particularly southeastern Australia, including Victoria, during 9–14 January 2011 (Fig. 2b, c). The strengthening of the extratropical low and associated heavy rainfall over southeastern Australia are consistent with southward advection of moisture by the meridional wind (Fig. 4) and Rossby wave interactions through the westerly zonal wind duct (Webster and Holton 1982; Frederiksen and Webster 1988; Moteki 2016).

These results in the wavenumber–frequency domain complement the synoptic analysis and are compared with our dynamical analyses in Sect. 6 of rapid growth of Kelvin waves convectively coupled to strong intra-seasonal oscillation (ISO) modes such as the MJO during the severe rainfall event in January 2011.

We have also analysed the behavior of the MJO during the northern winter and early spring of 2010–2011 through the MJO index of Wheeler and Hendon (2004). Their Real-Time Multivariate MJO (RMM) index characterizes the



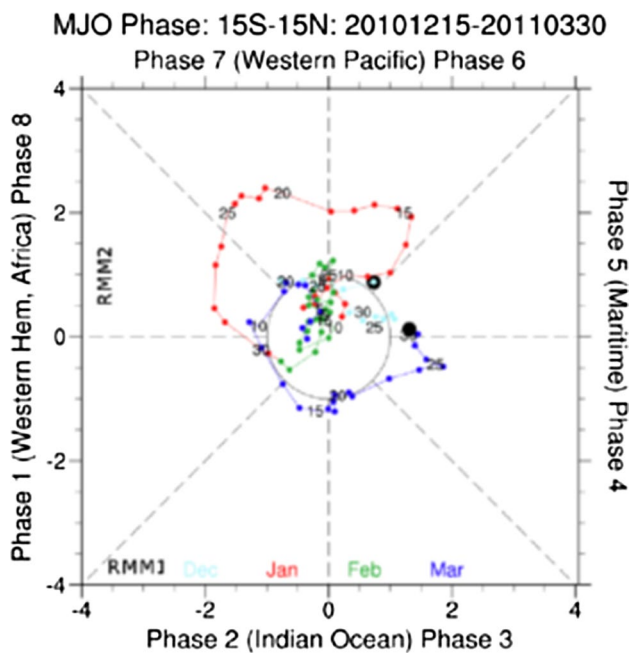


Fig. 6 The observed trajectory of the MJO index in the RMM1-RMM2 phase space for December 2010 (*light blue*), January (*red*), February (*green*) and March (*dark blue*) 2011, calculated from NCEP Reanalysis data. Strength of the MJO is indicated by the *line's* distance from the center. Strong growth can be seen in the Australian region (phase 5 and 6) in January

MJO by two leading EOFs (RMM1 and RMM2) of averaged (15N to 15S) OLR, 850 hPa zonal wind and 200 hPa zonal wind. The evolution of the MJO index in RMM1 and RMM2 space is shown in Fig. 6. We note the rapid growth of the MJO during January 2011 to maximum amplitude around 15 January. This occurs at phase 6 when the MJO convection and rainfall is a maximum over northern Australia on a climatological basis (Fig. 3 of Wheeler et al. 2009) and is again consistent with the extreme rainfall in Fig. 2c.

Oliver and Thompson (2012) used regression analysis to reconstruct the Wheeler and Hendon (2004) MJO index from 1905 to 2011 based on 20CRV2 data. Their reconstructed index again grows rapidly in magnitude during early January with the largest amplitudes (~ 2) between 5 and 10 January in 1974 and between 10 and 15 January in 2011 at phases 5 to 6 (not shown).

5 CSIRO Mk3L GCM simulations

For our simulation study, we chose the CSIRO Mk3L GCM for its computational efficiency as a spectral general circulation model and suitability for climate variability studies (Phipps 2010; Phipps et al. 2011). It maintains full atmospheric physics, enabling it to skilfully represent leading

modes of internal climate variability. It can be run either coupled or separately as an atmospheric or ocean simulation. Here, we have run the stand-alone Mk3L atmospheric model consisting of atmosphere, land surface and sea ice components. The atmosphere component's cumulus convection scheme is coupled to a prognostic stratiform cloud scheme (Gregory and Rowntree 1990; Rotstajn 2000). The radiation scheme can run both annual and diurnal cycles by calculating shortwave and longwave radiation separately every 2 h. The method of Cess and Potter (1987) is used for the calculation of cloud radiative forcings; clear-sky radiation calculations are performed at each timestep. The multi-layer dynamic-thermodynamic sea ice model describes ice in three layers, one for snow and two for ice, and allows fractional ice cover at sea ice gridpoints (O'Farrell 1998). The Kowalczyk et al. (1991, 1994) soil-canopy scheme is used as the basis for the land surface model. Mk3L consists of an 18 level hybrid vertical coordinate system with a horizontal resolution of R21 (5.625 degree zonal and 3.18 degree meridional resolution). To prevent decoupling at odd and even timesteps, the model uses a timestep of 20 min employing a semi-implicit leapfrog scheme with a Robert-Asselin time filter (Robert 1966).

The stand-alone Mk3L atmospheric model uses climatological ozone, CO₂ transmission coefficients and SST data from auxiliary files. For climatological ozone concentrations, we used the Atmospheric Model Intercomparison Project (AMIP II) recommended dataset (Wang et al. 1995). CO₂ data was a historical time-evolving data set (Meinshausen et al. 2011). We interpolated the observed monthly mean HADISST dataset ($1^\circ \times 1^\circ$) onto the Mk3L grid both spatially and temporally (per timestep) with no allowance for diurnal variation (Deser et al. 2010). We modified the stand-alone atmospheric Mk3L SST forcing to intake the observed monthly mean HADISST dataset, rather than climatological SST values.

5.1 Ensemble simulations

For the period of 1870–2011, we ran eight ensemble members (hereafter referred to as FORCED) plus a standard or baseline simulation (STD-FORCED), forcing both with the time-evolving CO₂ and HADISST data. The STD-FORCED run was initialized using the Mk3L default initial conditions (provided in a default restart file, the result of a 100 year spin-up run to bring the model to equilibrium for pre-industrial conditions). Each ensemble member was initialized with a new restart file (NRF) containing four perturbed atmospheric fields—pressure, streamfunction, velocity potential and temperature—according to the following equation:

$$\text{NRF} = \text{DRF} \pm [(\text{DRF} - \text{FRF}) * 0.1]$$

which represents taking a fraction of the differences between the default restart file (DRF) and one of four restart files (FRF) taken from different years of a control simulation run for 145 years with constant pre-industrial boundary conditions of climatological SSTs and CO₂ concentrations fixed at 280 ppm. To reduce variation between ensemble members, we substituted the daily thermodynamic sea ice model values of the STD-FORCED simulation into each member simulation of the FORCED ensemble.

Previous studies saw that Mk3L stand-alone atmosphere model ensembles with the thermodynamic sea ice model component ‘turned on’ can have quite large variations between their members despite relatively small perturbations in their initial conditions and long run periods (Freitas et al. 2015). To test whether controlling for the sea ice component might reduce this variation, we substituted the daily thermodynamic sea ice model values of the STD-FORCED simulation into each member simulation of the FORCED ensemble. Freitas et al. (2015) found that while this trial did reduce the variation between ensemble members, it did not do so significantly or significantly change the overall results. Here, we present the results for simulations that include this sea ice model data formulation.

Model simulations, with observed SSTs, from distant initial conditions, are unlikely to capture particular extreme weather events because of the chaotic nature of the atmospheric circulation. Nevertheless, some members of an ensemble may have qualitatively similar behaviour to observed events while others will deviate significantly. Here, we find that the STD-FORCED simulation is one of several that captures some of the broad features of the rainfall and weather events of January 1974 and 2011, albeit with some shifts in the timing.

The STD-FORCED OLR anomalies for January 2011 show a strong signal in the Mk3L model and in broad terms agree well with NCEP reanalysis OLR anomaly data (Fig. 7). We note the similarity of the OLR fields and precipitation for the observations (Figs. 7c, 9b) and the STD-FORCED simulation (Figs. 7d, 9a). There is of course considerable variability in the timing and areas of maximum precipitation between the FORCED ensemble members (Figs. 9c, 11). Although all displayed anomalous precipitation near northern Australia during the late December to early February time period, a few members located the highest precipitation offshore. Variability was also high in the wavenumber–frequency filtering of the ensemble simulations. While the Kelvin wave and MJO reinforce convection in the Mk3L STD-FORCED simulation (albeit in late January (Fig. 5b)), some ensemble members did not capture the constructive interference (not shown). This variability underscores that severe weather events with the highest impacts often result from the particular timing and interference of multiple elements.

The NCEP and STD-FORCED simulation OLR anomalies for the northern winter of 1973–1974 are shown in Fig. 8, and the associated precipitation fields for January 1974 are shown in Fig. 10. Again, peak precipitation is associated with negative OLR anomalies. The Hovmöller diagram in Fig. 5c shows considerable MJO activity in the vicinity of northern Australia during January 1974, consistent with the reconstructed MJO index discussed in Sect. 2. As well, we note the reinforcement of MJO convection by Kelvin waves both early and mid-month. The variance of the rainfall for the FORCED ensemble members in Fig. 10c indicates the considerable variability between simulations (Figs. 9, 10, 11).

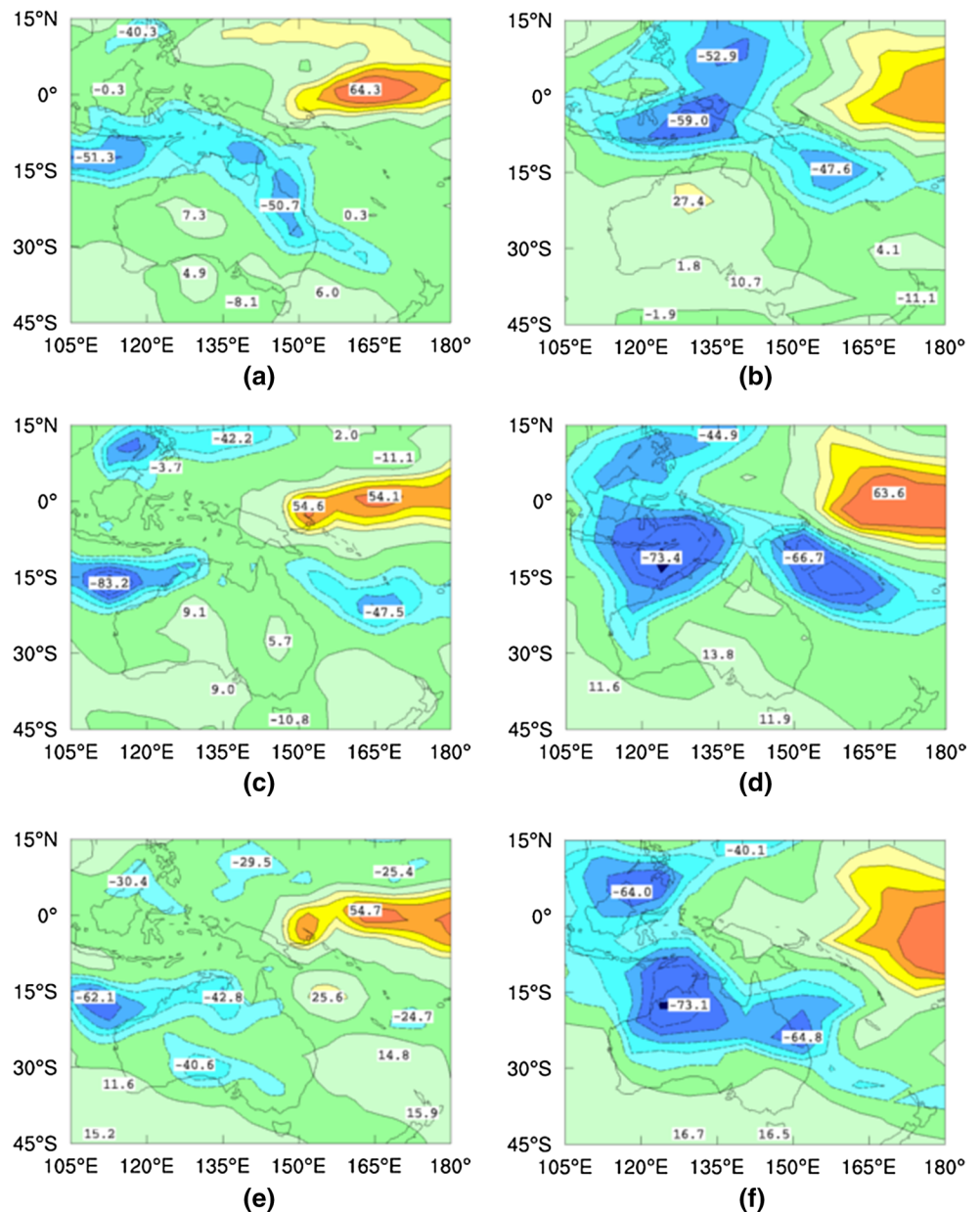
6 Dynamical modes in a primitive equation model

Next, we examine important fast-growing dynamical modes during January 1974 and 2011 using a two-level primitive equation instability model. Full details of the version of the model used are given in Frederiksen and Frederiksen (2007). Here we briefly summarize our approach for calculating dynamical modes.

The primitive equations are formulated in terms of the mean (average of the upper, 300 hPa, and lower, 700 hPa level) and shear (half the difference between the upper and lower levels) streamfunctions, the mean and shear potential temperatures and the lower level velocity potential (equal to minus the upper-level velocity potential). We used a generalized Kuo-type heating parameterization (Kuo 1974) with closures for cumulus convection and evaporation–wind feedback. The model also includes drag and biharmonic diffusion. The equations are linearized about the reanalyzed January 1974 and 2011 monthly three-dimensional basic states. We expanded the basic states and perturbations in terms of spherical harmonics with the perturbations having a time dependence $\exp(-i\omega t)$. Here, t is the time and $\omega = \omega_r + i\omega_i$ consists of the frequency ω_r and the growth rate ω_i . This then results in a system of eigenvalue–eigenvector equations (Frederiksen and Frederiksen 1992) for the five perturbation fields.

In our current calculations we use the same strengths of the convection, evaporation–wind feedback, drag, diffusion and resolution as for the EVAP basic state in appendix B of Frederiksen and Lin (2013). Here the periods of the modes are given as $T = 2\pi/\omega_r$ and e-folding time is $\tau = \omega_i^{-1}$. We solve the eigenvalue–eigenvector equations of the eigenvalues $\omega = \omega_r + i\omega_i$ and eigenvectors giving the structures of the dynamical modes. The modes are sorted by the growth rates with the fastest growing disturbance labeled mode 1 and mode N having the Nth largest growth rate.

Fig. 7 OLR anomalies (Wm^{-2}) from NCEP (left column) and Mk3L STD-FORCED simulation (right column) for December 2010 (a and b), January 2011 (c and d) and February 2011 (e and f). Contour interval: 10 Wm^{-2} . The Mk3L model captures, with some overestimation in extent and duration, the areas of strong convection



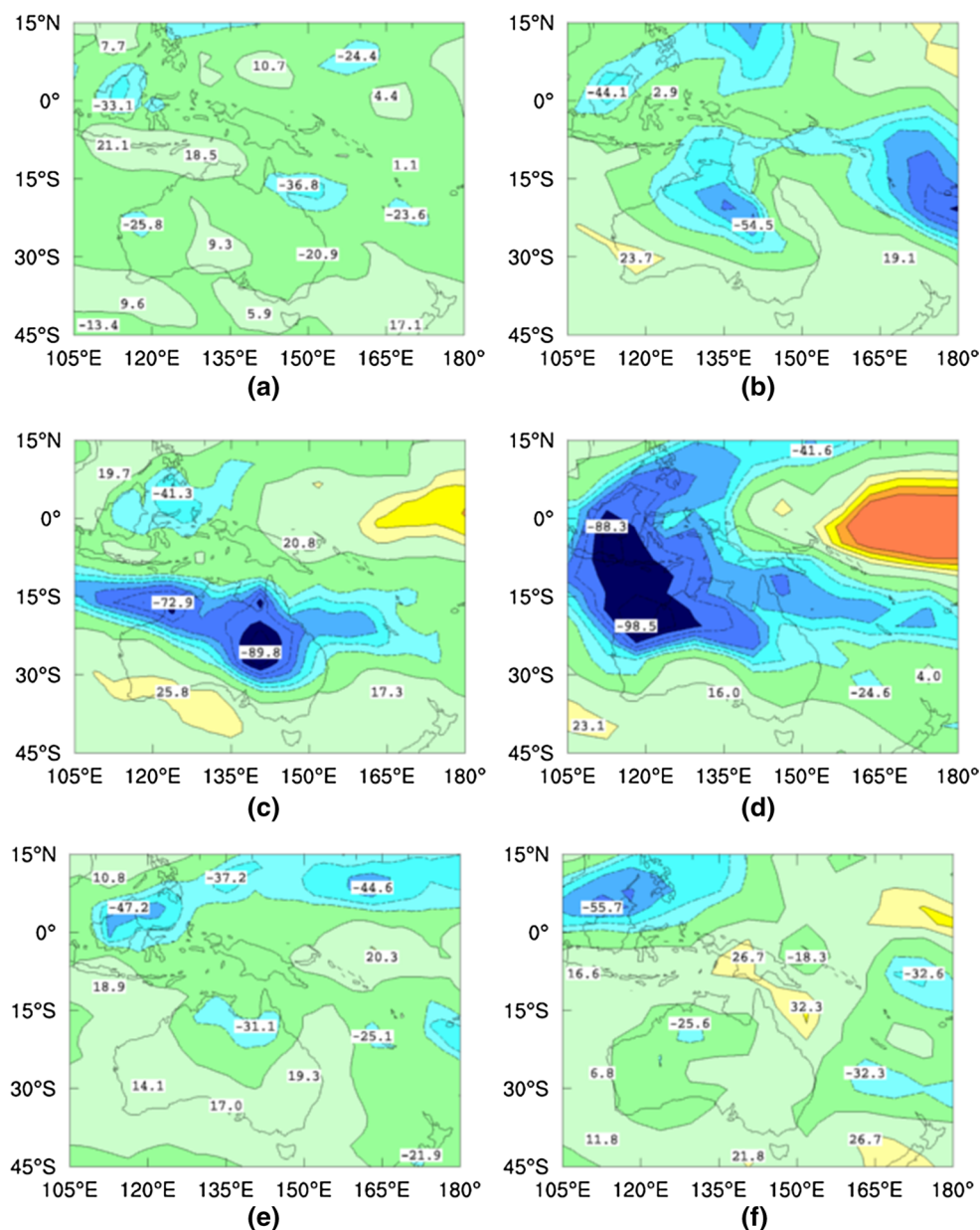
6.1 Dynamical modes associated with La Niña during January 1974

Typically relatively small scale modes, such as storm track modes, usually have the largest growth rates in instability calculations while in nonlinear integrations (Frederiksen 1981) the larger scale modes reach larger amplitudes. This is also the case for the January 1974 basic state where the fastest growing mode is a Northern Hemisphere cyclogenesis modes with largest amplitudes in the Pacific and Atlantic storm tracks. Modes 3 and 4 are Southern Hemisphere cyclogenesis modes with mode 3 having a period of $T = 1.8$ days and an e-folding time of $\tau = 2.1$ days. At both upper and lower levels its streamfunction has significant

amplitude across southern Australia (not shown) and is very similar to that of mode 1 for 1949–1968, shown in Frederiksen et al. (2011, Fig. 1 top panel). This contrasts with the leading Southern Hemisphere mode (mode 1) for 1997–2006 (shown in in bottom panel of same figure), when southern Australia experienced the Millennium Drought, associated with a number of El Niño events.

Consistent with the Hovmoller diagrams and the synoptic analysis of Sect. 4, the January 1974 basic state also results in explosive growth of Kelvin waves with the leading wave (mode 17) having a period of $T = 15.6$ days and an e-folding time of $\tau = 3.3$ days; this corresponds to a growth rate that is around four times faster than that for the leading Kelvin wave for the January 1979 basic state in the study of

Fig. 8 As in Fig. 7 for December 1973 (a and b), January 1974 (c and d) and February 1974 (e and f)



Frederiksen (2002; Table 1, EVAP basic state). That paper discusses the properties of Kelvin waves in more detail.

The 300 hPa streamfunction and velocity potential for the leading January 1974 Kelvin wave are shown in Fig. 12a, b. We note that, at the phase shown, there is a large negative anomaly of the streamfunction centered over northwest Australia and a negative velocity potential anomaly over northern Australia that corresponds to large scale convective uplift and precipitation.

Associated with the La Niña of January 1974, there is also a group of fast growing intraseasonal oscillation (ISO) modes with periods between 30 and 60 days and e-folding times of between 4.1 and 4.7 days. The fastest growing is mode 37 which has a period of $T = 30$ days and an e-folding

time of $\tau = 4.7$ days; the corresponding growth rate is thus circa 70% greater than for the leading ISO mode of the January 1979 basic state of Frederiksen (2002) and the January 1988 basic state of Frederiksen and Lin (2013), and more than double that for their January 1980–2009 basic state. The 300 hPa streamfunction and velocity potential for ISO mode 37 for January 1974 are shown in Fig. 12c, d. We see that, at the phase shown, there are negative streamfunction anomalies across northern and western Australia and positive anomalies centered over the southeast coast. Importantly, the velocity potential shows a band of negative anomalies particularly across northern Australia to the maritime continent; again this is consistent with the convective uplift and precipitation across northern Australia and the maritime continent.

Fig. 9 Precipitation (mm/day) for January 2011 from **a** STD-FORCED simulation, **b** NCEP reanalysis and **c** variance of precipitation (mm/day)² from FORCED ensemble. Members varied significantly in the timing and location of the high rainfall event. Contour interval: 5 mm

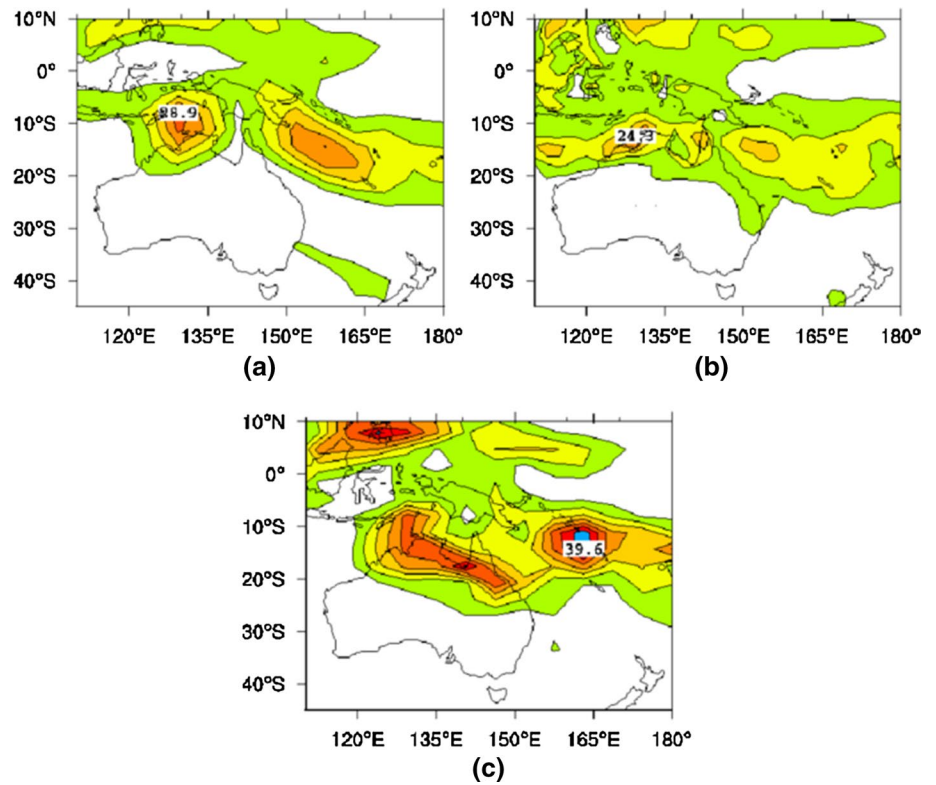
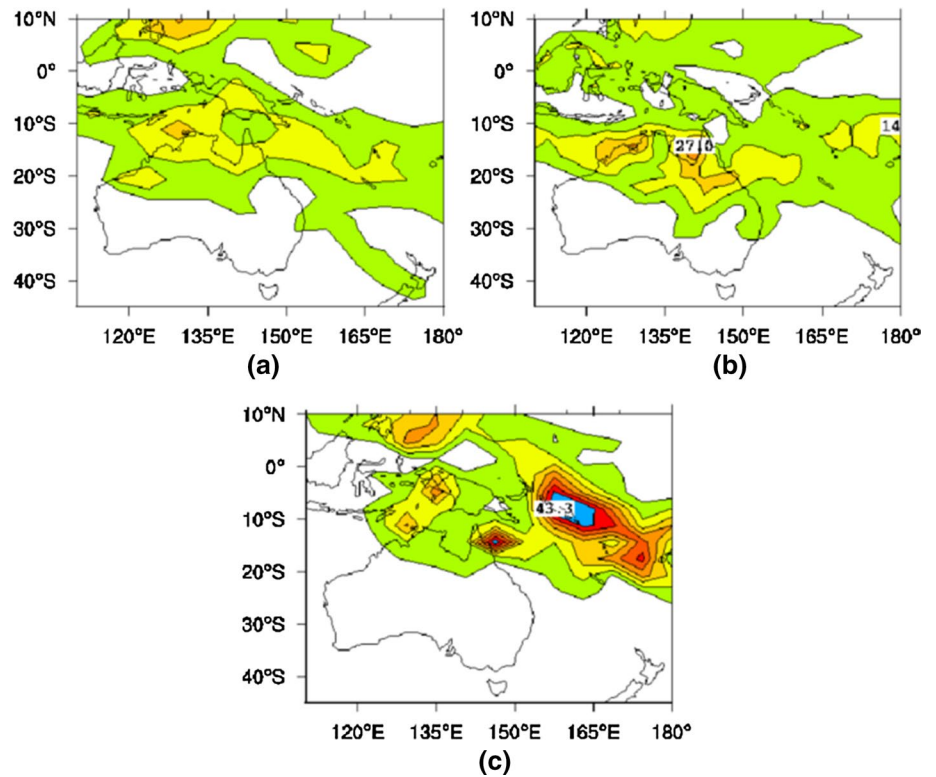


Fig. 10 As in Fig. 9 for January 1974. Contour interval: 5 mm



The studies of Frederiksen and Frederiksen (1993, 1997) also found quasi-stationary monsoon modes located in the Australian region during January 1979. This is also the

case for the January 1974 basic state with mode 62 having a period of $T = \infty$ and an e-folding time of $\tau = 6.4$ days and with structure in the Australian region similar to that

Fig. 11 January 2011 precipitation (mm/day) in two different FORCED ensemble member simulations. These two realizations, along with the STD-FORCED simulation (Fig. 9), show high levels of daily precipitation over northeastern Australia. Contour interval: 5 mm

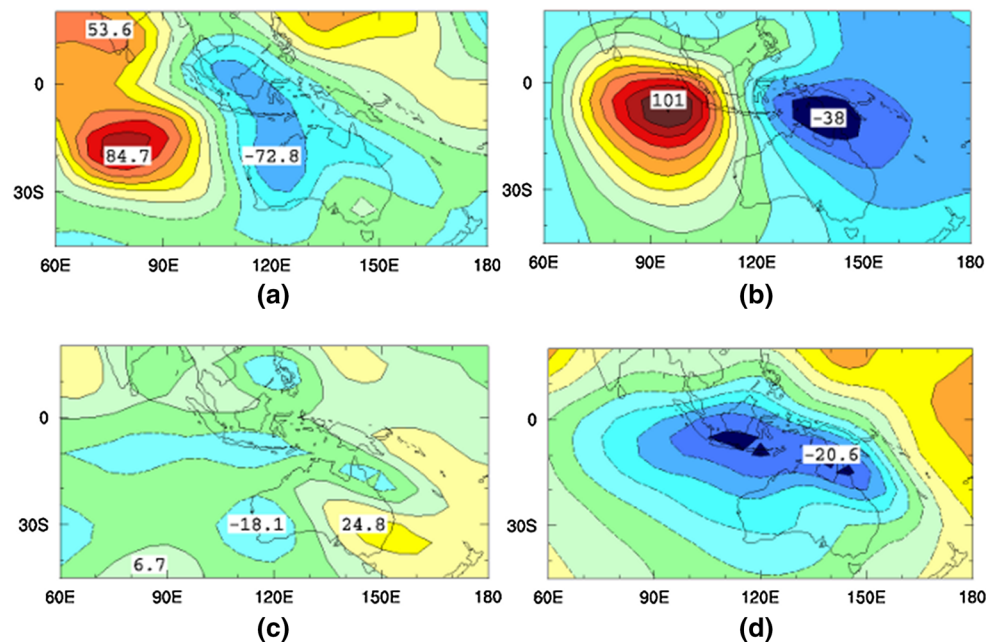
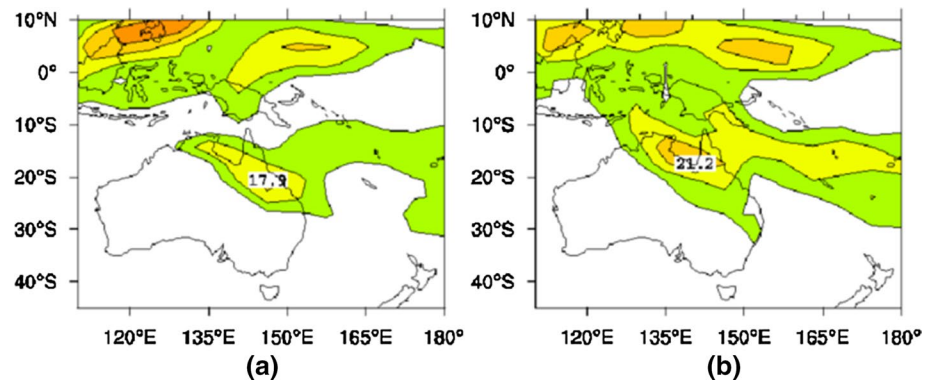


Fig. 12 January 1974 **a** 300 hPa streamfunction and **b** velocity potential of dominant Kelvin wave mode, **c** 300 hPa streamfunction and **d** velocity potential of the leading intraseasonal oscillation mode. The modes have arbitrary units and contour intervals are 15, 10, 10 and 3, respectively

shown in Fig. 5 of Frederiksen and Frederiksen (1993) with convective uplift and precipitation over northern Australia.

6.2 Dynamical modes associated with La Niña during January 2011

The similarities during January 1974 and 2011 between the atmospheric circulations, OLR, rainfall and observed and modeled MJO and Kelvin waves described in previous sections are reflected in the dynamical modes for the two periods. During January 2011, the leading Southern Hemisphere storm track mode is mode 3 with a period of $T = 1.7$ days and an e-folding time of $\tau = 1.7$ days. Again it has significant streamfunction amplitude across southeastern Australia and this is also the case for many of the slower growing storm track modes (not shown).

The leading Kelvin wave for the January 2011 basic state (mode 28 with $T = 18.4$ days and $\tau = 4.2$ days) grows a little slower than that for January 1974 but nevertheless around three times faster than that for January 1979 (Frederiksen 2002, EVAP basic state). The leading January 2011 ISO mode is mode 46 with $T = 47.7$ days and $\tau = 5.8$ days and it grows circa 40% faster than the corresponding ISO mode for January 1979 (Frederiksen 2002, EVAP basic state). The leading Kelvin wave and ISO mode for January 2011 are very similar in structure, at the corresponding phase, to those shown in Fig. 12 (Whelan et al. 2013, Figs. 3 and 4). For both periods the center of the negative 300 hPa velocity potential of the leading Kelvin wave mode (Fig. 12b) responding to the local SSTs is displaced to $\sim 10^\circ\text{S}$ compared to the equatorial location of the center for the Kelvin wave in

Figure 8a of Frederiksen (2002). Although there is no simple relationship between the growth rate of small amplitude disturbances and the amplitude that they can reach (Frederiksen 1981), we note that the observed MJO did grow quite rapidly during the first half of January 2011 (Fig. 6) and January 1974. The leading monsoon disturbance in the Australian region is mode 47 with a period of $T = \infty$ and an e-folding time of $\tau = 5.8$ days, which again is consistent with the rainfall anomalies during January 2011.

7 Conclusions

We find that the extreme flooding event over northern and eastern Australia in January 1974 and 2011 coincided with significant intraseasonal oscillation and Kelvin wave activity that constructively interfered on the critical days of heavy rainfall. An explosive Kelvin wave arrived over northern Australia at the right time to become convectively coupled in the Australian monsoon region, enhancing convection. At the same time, a strongly growing intraseasonal MJO moved through the region. Blocking high pressure systems in the Tasman Sea and unstable easterly winds associated with the low pressure served to prevent precipitation conditions from moving off the Australian coast. We find that for some Mk3L simulations, both the timing and patterns of the dynamical modes are consistent with the synoptic situation seen in observations. The analyses in this paper seem to offer novel insights into the factors behind the intense rainfall and flooding events.

Dynamical modes associated with these flooding events have been determined using a primitive equation instability model. We find that heavy rainfall is associated with increased growth rates of Kelvin waves, intraseasonal oscillations (ISO), monsoon disturbances, and associated blocking over the Tasman Sea, as well as some changes in the extratropical storm track modes. In particular, we find that the MJO and Kelvin waves grow explosively and are strongly convectively coupled in the Australian monsoonal region, enhancing convection over Australia. Tropical–extratropical interactions also play important roles in the severe rainfall and flooding events. We find similar Kelvin waves and monsoonal modes in both events, although in 1974 both were slightly stronger than in 2011. Our dynamical analyses agree with the synoptic observations and provide a more complete description of the reasons for the severity of both events.

Acknowledgements We thank Matt Wheeler for helpful suggestions regarding this study, Steven Phipps for assistance with the CSIRO Mk3L model, and Stacey Osbrough for assistance with graphics. JW thanks the CSIRO Office of the Chief Executive for the award of a Postdoctoral Fellowship.

References

- Ashok K, Guan Z, Yamagata T (2003) Influence of the Indian Ocean Dipole on the Australian winter rainfall. *Geophys Res Lett* 30(15):1821. doi:10.1029/2003GL017926
- Australian Bureau of Meteorology. Record-breaking La Niña events: an analysis of the La Niña: a life cycle and the impacts and significance of the 2010–11 and 2011–12 La Niña events in Australia. <http://www.bom.gov.au/climate/enso/history/La-Nina-2010-12.pdf>
- Brown J, Mcintosh PC, Pook MJ, Risbey JS (2009) An investigation of the links between ENSO flavors and rainfall processes in southeastern Australia. *Mon Weather Rev* 137(11):3786–3795
- Cai W, Cowan T (2009) La Niña Modoki impacts Australian autumn rainfall variability. *Geophys Res Lett* 36:L12805. doi:10.1029/2009GL037885
- Cai W, van Rensch P (2012) The 2011 southeast Queensland extreme summer rainfall: a confirmation of a negative Pacific Decadal Oscillation phase? *Geophys Res Lett* 39:L08702
- Cess RD, Potter GL (1987) Exploratory studies of cloud radiative forcing with a general circulation model. *Tellus* 39A:460–473
- Compo GP, Whitaker JS, Sardeshmukh PD et al (2011) The twentieth century reanalysis project. *Q J R Meteorol Soc* 137:1–28
- Deser C, Phillips AS, Alexander MA (2010) Twentieth century tropical sea surface temperature trends revisited. *Geophys Res Lett* 37:L10701
- Evans JP, Boyer-Souchet I (2012) Local sea surface temperatures add to extreme precipitation in northeast Australia during La Niña. *Geophys Res Lett* 39:L10803
- Frederiksen JS (1981) Scale selection and energy spectra of disturbances in Southern Hemisphere flows. *J Atmos Sci* 38:2573–2584
- Frederiksen JS (2002) Genesis of intraseasonal oscillations and equatorial waves. *J Atmos Sci* 59:2761–2781
- Frederiksen CS, Frederiksen JS (1992) Northern hemisphere storm tracks and teleconnection patterns in primitive equation and quasi-geostrophic models. *J Atmos Sci* 39:1443–1458
- Frederiksen JS, Frederiksen CS (1993) Monsoon disturbances, intraseasonal oscillations, teleconnection patterns, blocking and storm tracks of the global atmosphere during January 1979: linear theory. *J Atmos Sci* 50:1349–1372
- Frederiksen JS, Frederiksen CS (1997) Mechanisms of the formation of intraseasonal oscillations and Australian monsoon disturbances: the roles of convection, barotropic and baroclinic instability. *Contrib Atmos Phys* 70:39–56
- Frederiksen JS, Frederiksen CS (2005) Decadal changes in Southern Hemisphere winter cyclogenesis. CSIRO Marine and Atmospheric Research Paper No. 002, Aspendale, VIC: CSIRO Marine and Atmospheric Research. V, 29p. http://www.cmar.csiro.au/e-print/open/frederiksenjs_2005b.pdf
- Frederiksen JS, Frederiksen CS (2007) Interdecadal changes in southern hemisphere winter storm track modes. *Tellus* 59A:599–617
- Frederiksen JS, Frederiksen CS (2011) Twentieth century winter changes in Southern Hemisphere synoptic weather modes. *Adv Meteorol.* Article ID 353829, 16pp. doi:10.1155/2011/353829
- Frederiksen JS, Lin H (2013) Tropical–extratropical interactions of intraseasonal oscillations. *J Atmos Sci* 70:3180–3196
- Frederiksen JS, Webster PJ (1988) Alternative theories of atmospheric teleconnections and low-frequency fluctuations. *Rev Geophys* 26:459–494
- Frederiksen JS, Frederiksen CS, Osbrough SL, Sisson JM (2011) Changes in southern hemisphere rainfall, circulation and weather systems. MODSIM2011, pp 2712–2718. ISBN: 978-0-9872143-1-7. www.mssanz.org.au/modsim2011/F5/frederiksen.pdf

- Freitas ACV, Frederiksen JS, Whelan J, O’Kane TJ, Ambrizzi T (2015) Observed and simulated inter-decadal changes in the structure of Southern Hemisphere large-scale circulation. *Clim Dyn* 45:2993–3017
- Gregory D, Rowntree RP (1990) A mass flux convection scheme with representation of cloud ensemble characteristics and stability-dependent closure. *Mon Weather Rev* 118:1483–1506
- Hendon HH, Wheeler MC, Zhang C (2007) Seasonal dependence of the MJO-ENSO relationship. *J Clim* 20:531–543
- Jones DA, Wang W, Fawcett R (2009) High-quality spatial climate data-sets for Australia. *Aust Meteorol Oceanogr* 58:233–248
- Kalnay E et al (1996) The NCEP/NCAR 40-year reanalysis project. *Bull Am Meteorol Soc* 3:437–471
- Karoly DJ (1989) Southern Hemisphere circulation features associated with El Niño-Southern Oscillation events. *J Clim* 2:1239–1252
- Kowalczyk EA, Garratt JR, Krummel PB (1991) A soil-canopy scheme for use in a numerical model of the atmosphere—1D stand-alone model. Technical Report 23, CSIRO Division of Atmospheric Research
- Kowalczyk EA, Garratt JR, Krummel PB (1994) Implementation of a soil-canopy scheme into the CSIRO GCM—regional aspects of the model response. Technical Report 32, CSIRO Division of Atmospheric Research
- Kuo HL (1974) Further studies of the parameterization of the influence of cumulus convection on large scale flow. *J Atmos Sci* 31:1232–1240
- Leonard M, Westra S, Phatak A, Lambert M, van den Hurk B, McInnes K, Risbey J, Schuster S, Jakob D, Stafford-Smith M (2013) A compound event framework for understanding extreme impacts. *WIREs Clim Change*. doi:10.1002/wcc.252
- Lewis S, Karoly DJ (2015) Are estimates of anthropogenic and natural influences on Australia’s extreme 2010–2012 rainfall model-dependent? *Clim Dyn* 45:679–695
- L’Heureux ML, Thompson DWJ (2006) Observed relationships between the El Niño-Southern Oscillation and the extratropical zonal-mean circulation. *J Clim* 19:276–287
- Liebmann B, Smith CA (1996) Description of a complete (interpolated) outgoing longwave radiation dataset. *Bull Am Meteorol Soc* 77:1275–1277
- Madden RA, Julian PR (1971) Detection of a 40–50 day oscillation in the zonal wind in the tropical Pacific. *J Atmos Sci* 28:702–708
- Madden R, Julian PR (1994) Observations of the 40–50 day tropical oscillation: a review. *Mon Weather Rev* 122:814–837
- McBride JL, Nicholls N (1983) Seasonal relationships between Australian rainfall and the Southern Oscillation. *Mon Weather Rev* 111:1998–2004
- Meinshausen M et al (2011) The RCP greenhouse gas concentrations and their extensions from 1765 to 2300. *Clim Change* 109:213–241. doi:10.1007/s10584-011-0156-z
- Meyers G, McIntosh P, Pigot L, Pook M (2007) The years of El Niño, La Niña, and interactions with the tropical Indian Ocean. *J Clim* 20:2872–2880
- Moon J-Y, Wang B, Ha K-J (2011) ENSO regulation of MJO teleconnection. *Clim Dyn* 37:1133–1149
- Moteki Q (2016) Propagation processes of the Madden-Julian Oscillation synchronized with an extratropical cyclone observed in late October during CINDY2011. *SOLA* 12:60–64
- Nicholls N (1989) Sea surface temperature and Australian winter rainfall. *J Clim* 2:965–973
- Nicholls N, Drosowsky W, Lavery B (1997) Australian rainfall variability and change. *Weather* 52:66–71
- O’Farrell SP (1998) Investigation of the dynamic sea ice component of a coupled atmosphere-sea ice general circulation model. *J Geophys Res* 103(C8):15751–15782
- Oliver ECJ, Thompson KR (2012) A reconstruction of Madden-Julian Oscillation variability from 1905 to 2008. *J Clim* 25:1996–2019. <http://passage.phys.ocean.dal.ca/~olivere/histmjo.html>
- Pezza AB, Durrant T, Simmonds I, Smith I (2008) Southern hemisphere synoptic behavior in extreme phases of SAM, ENSO, sea ice extent, and southern Australia rainfall. *J Clim* 21(21):5566–5579
- Philander SG (1990) *El Niño, La Niña, and the Southern Oscillation*. Academic Press, New York
- Phipps J (2010) The CSIRO Mk3L climate system model v1. 2. Technical Report No. 4, Antarctic Climate & Ecosystems CRC, Hobart, Tasmania, Australia, p 12
- Phipps SJ, Rotstayn LD, Gordon HB, Roberts JL, Hirst AC, Budd WF (2011) The CSIRO Mk3L climate system model version 1.0—Part 1: description and evaluation. *Geosci Model Dev* 4:483–509
- Risbey JS, Pook MJ, McIntosh PC, Wheeler MC, Hendon HH (2009) On the remote drivers of rainfall variability in Australia. *Mon Weather Rev* 137:3233–3253
- Robert AJ (1966) The integration of a low order spectral form of the primitive meteorological equations. *J Meteorol Soc Jpn* 44:237–244
- Rotstayn LD (2000) On the “tuning” of autoconversion parameterizations in climate models. *J Geophys Res* 105:15495–15507
- Taschetto AS, England MH (2009) El Niño Modoki impacts on Australian rainfall. *J Clim* 22:3167–3174
- Ummenhofer CC, Sen Gupta A, England MH, Taschetto AS, Briggs PR, Raupach MR (2015) How did ocean warming affect Australian rainfall extremes during the 2010/2011 La Niña event? *Geophys Res Lett* 42:9942–9951
- Wang G, Hendon HH (2007) Sensitivity of Australian rainfall to inter-El Niño variations. *J Clim* 20:4211–4226
- Wang W-C, Liang X-Z, Dudek MP, Pollard D, Thompson SL (1995) Atmospheric ozone as a climate gas. *Atmos Res* 37:247–256
- Webster PJ, Holton JR (1982) Cross-equatorial response to mid-latitude forcing in a zonally varying basic state. *J Atmos Sci* 39:722–733
- Wheeler M, Hendon H (2004) An all-season real-time multivariate MJO index: development of an index for monitoring and prediction. *Mon Weather Rev* 132:1917–1932
- Wheeler M, Kiladis GN (1999) Convectively coupled equatorial waves: analysis of clouds and temperatures in the wavenumber-frequency domain. *J Atmos Sci* 56:374–398
- Wheeler MC, Hendon HH, Cleland S, Meinke H, Donald A (2009) Impacts of the Madden-Julian Oscillation on Australian rainfall and circulation. *J Clim* 22:1482–1498
- Whelan JA, Frederiksen JS (2015) Simulations of Australian extreme rainfall and circulation during the January 2011 La Niña. ANZIAM J, Proceedings of the 17th biennial computational techniques and applications conference, CTAC-2014, 56, pp C179–C193. <http://journal.austms.org.au/ojs/index.php/ANZIAMJ/article/view/9353>
- Whelan JA, Frederiksen JS, Frederiksen CS, Osbrough SL (2013) Synoptic and dynamical analyses of ENSO extreme events over Australia. MODSIM2013, 20th international congress on modelling and simulation. Modelling and Simulation Society of Australia and New Zealand, Dec 2013, pp 2590–2596. ISBN: 978-0-9872143-3-1. www.mssanz.org.au/modsim2013/L7/whelan.pdf